

Comparison of Short-Range Order in GeSn Grown by Molecular Beam Epitaxy and Chemical Vapor Deposition

Shang Liu^{1†}, Yunfan Liang^{2†}, Haochen Zhao³, Nirosh M. Eldose⁴,
Jin-Hee Bae⁵, Omar Concepcion⁵, Xiaochen Jin⁶, Shunda Chen⁶,
Ilias Bikhmetov⁷, Austin Akey⁸, Cory T. Cline¹,
Alejandra Cuervo Covian¹, Xiaoxin Wang¹, Tianshu Li⁶,
Yuping Zeng³, Dan Buca³, Shui-Qing Yu⁹, Gregory J. Salamo⁴,
Shengbai Zhang², Jifeng Liu^{1*}

¹Thayer School of Engineering, Dartmouth College, Hanover, 03755,
NH, USA.

²Department of Physics, Applied Physics and Astronomy, Rensselaer
Polytechnic Institute, Troy, 12180, NY, USA.

³Department of Electrical and Computer Engineering, University of
Delaware, Newark, 19716, DE, USA.

⁴Institute for Nanoscience and Engineering, University of Arkansas,
Fayetteville, 72701, AR, USA.

⁵Peter Gruenberg Institute 9 (PGI-9), Forschungszentrum Juelich,
Juelich, 52428, Germany.

⁶Department of Civil and Environmental Engineering, George
Washington University, Washington, 20052, DC, USA.

⁷Department of Metallurgical & Materials Engineering, University of
Alabama, Tuscaloosa, 35405, AL, USA.

⁸Center for Nanoscale Systems, Harvard University, Cambridge, 02138,
MA, USA.

⁹Department of Electrical Engineering, University of Arkansas,
Fayetteville, 72701, AR, USA.

*Corresponding author(s). E-mail(s): Jifeng.Liu@dartmouth.edu;

†These authors contributed equally to this work.

Abstract

Atomic short-range order (SRO) in direct-bandgap GeSn for infrared photonics has recently attracted attention due to its notable impact on band structures. However, the SRO in GeSn thin films grown by different methods have hardly been compared. This paper compares SRO in GeSn thin films of similar compositions grown by molecular beam epitaxy (MBE) and chemical vapor deposition (CVD) using atom probe tomography. An $\sim 15\%$ stronger preference for Sn-Sn 1st nearest neighbor (1NN) is observed in MBE GeSn than CVD GeSn for both thin film and quantum well samples with Sn composition ranging from 7 to 20%. Interestingly, samples grown by different deposition tools under the same method (either MBE or CVD) showed remarkable consistency in Sn-Sn 1NN SRO, while MBE vs. CVD showed clear differences. Supported by theoretical modeling, we consider that this difference in SRO originates from the impact of surface termination, where MBE surfaces are exposed to ultrahigh vacuum while CVD surfaces are terminated by H to a good extent. This finding not only suggests engineering surface termination or surfactants during the growth as a potential approach to control SRO in GeSn, but also provides insight into the underlying reasons for very different growth temperature between MBE and CVD that directly impact the strain relaxation behavior.

Keywords: Short-range order, GeSn alloys, atom probe tomography, Poisson statistics, K-th nearest neighbors (KNN), molecular beam epitaxy (MBE), chemical vapor deposition (CVD)

1 Introduction

GeSn is a promising candidate for Si-compatible direct-bandgap infrared optoelectronics.[1–8] In order to reduce threshold of GeSn lasers and dark current in GeSn image sensors, many recent studies have focused on defect and strain managements,[9–13] which requires a deeper insight into the crystal growth mechanism of GeSn. Molecular beam epitaxy (MBE) and chemical vapor deposition (CVD) are the most common techniques to grow GeSn thin films on Ge substrate or Ge-buffered Si substrate,[14–19] but their growth temperature windows and the corresponding strain relaxation kinetics are dramatically different. With a low deposition rate in ultrahigh vacuum in MBE, low temperature ($<200^\circ\text{C}$) is required to avoid Sn segregation. Although uniform [20] and high Sn composition up to 27% [21] has been demonstrated using MBE, fully relaxed and thick GeSn film has not been achieved yet due to the epitaxial breakdown caused by the kinetic roughening.[22] On the other hand, higher growth rate is allowed in CVD at higher temperature ranging from 250 to 400°C. Up to 22% Sn was accomplished by a spontaneous-relaxation-enhanced (SRE) Sn incorporation process in CVD,[5] although this process naturally introduce a composition gradient. Moreover, a self-organized dislocation network is localized to the region near GeSn/Ge interface, leaving the upper region relatively low in defect density.[11]

To investigate why lower growth temperature is required to suppress Sn segregation in MBE but higher growth temperature is allowed in CVD, a deep dive into nano-scale atomic configuration in GeSn is desired. Atomic short-range ordering (SRO) in GeSn has recently attracted attention due to its notable impact on band structures and thermal conductivity.[23, 24] For example, theoretical calculation predicts a lack of Sn-Sn nearest neighbors in GeSn alloys and this SRO leads to ~ 0.1 eV, ~ 0.16 eV and ~ 0.33 eV larger direct bandgap in $\text{Ge}_{0.875}\text{Sn}_{0.125}$, $\text{Ge}_{0.8125}\text{Sn}_{0.1875}$ and $\text{Ge}_{0.75}\text{Sn}_{0.25}$, respectively, compared to random alloys.[23, 25] So far, SRO in GeSn has been experimentally characterized using Extended X-ray Absorption Fine Structure (EXAFS) and atom probe tomography (APT), but the SRO in GeSn thin films grown by CVD and MBE have hardly been directly compared. Two papers reported that EXAFS shows deficiency of Sn-Sn bond in GeSn grown by CVD, but one of them is limited by a narrow k-range and impacted by localized amorphous regions,[26] while the other is on Ge/GeSn core/shell nanowires instead of thin films.[27] An early paper published EXAFS results of a GeSn thin film grown by MBE, but the coordination number around a Sn atom is larger than 4 from the fitting, which is physically impossible, while no fitting of Sn-Sn peak was performed.[28] Indeed, the fitting in EXAFS is sophisticated and it is nontrivial to distinguish a weak Sn-Sn signal from a strong Sn-Ge signal. Furthermore, EXAFS only gives averaged SRO in a relatively large area and cannot show SRO distribution in nano-scale, which is important to characterize SRO in GeSn.[29] By comparison, APT can measure SRO in real space [30] and provide nano-scale mapping of SRO with refined data analyses,[30] although it is more suitable for relative comparison of SRO rather than obtaining accurate SRO parameters due to the perturbation of atomic positions in the measurements. To date, no APT-based analysis of SRO in GeSn grown by MBE has been reported yet. Although ideally APT can probe position of each atoms and identify their species, its spatial resolution for semiconductor is low and the detection efficiency is also low. Thus conventional methods such as Fourier transform,[31] radial distribution function [32] and spatial distribution mapping [33] could not show clear features of the 1st, 2nd and 3rd nearest neighbors from APT data of GeSn or SiGeSn. Recently, to overcome these limitations, a Poisson-KNN method was developed to statistically reconstruct Kth nearest neighbor (KNN) from APT data of GeSn.[30]

Here, we utilized this Poisson-KNN method to compare the SRO in GeSn grown by MBE and CVD. An $\sim 15\%$ stronger preference of Sn-Sn 1NN is observed in GeSn grown by MBE, either in GeSn thin films or GeSn MQW samples. Supported by Density Functional Theory (DFT) modeling, we consider that this difference in SRO originates from the impact of surface termination, where MBE surfaces are exposed to ultrahigh vacuum while CVD surfaces are terminated by H to a good extent. The differences in surface termination directly impact the preference of Sn-Sn 1NN at the growth front, thereby modifying the overall Sn-Sn 1NN SRO parameter. This finding not only suggests engineering surface termination or surfactants during the growth as a potential approach to control SRO in GeSn, but also provides some insight into the underlying reasons for very different growth temperature between MBE and CVD that directly impact the strain relaxation behavior.

2 Results and discussion

2.1 APT data

APT data of four GeSn samples were analyzed. Sample #1 and #2 were grown by MBE, with 20% and 7% Sn, respectively. They were grown by two different MBE deposition tools at University of Delaware and University of Arkansas, respectively. Sample #3 and #4 were grown by CVD, with 14% and 7% Sn, respectively. They were grown by two different CVD reactors at University of Arkansas and Forschungszentrum Juelich, respectively. Moreover, sample #1 and #3 are GeSn thin films grown on a Ge substrate, while sample #2 and #4 are GeSn/Ge multiple quantum wells (MQW). The growth method and atomic composition are tabulated in Table 1.

Table 1 Growth method and composition

Sample #	Growth method	Ge (at.%)	Sn (at.%)	Structure
1	MBE	80	20	Thin film
2		93	7	MQW
3	CVD	86	14	Thin film
4		93	7	MQW

APT data of sample #1, #2 and #4 are presented in Fig. 1. Fig. 1a, d, g are composition profiles of these three samples derived from their APT data; Fig. 1b, e, h are reconstructed APT data; Fig. 1c, f, i are SRO mappings which will be explained in later sections. APT data of sample #3 has been published in Ref. [30] and therefore not repeated here.

2.2 SRO parameter definition

The experimental SRO parameter is defined as:

$$\alpha_{A-B}^{KNN} = \frac{P_{A-B}^{KNN}}{x_B} \begin{cases} > 1, & B \text{ atoms are favored in the } K^{\text{th}} \text{ shell of } A \text{ atom} \\ = 1, & \text{random alloy} \\ < 1, & B \text{ atoms are not favored in the } K^{\text{th}} \text{ shell of } A \text{ atom} \end{cases}, \quad (1)$$

where P_{A-B}^{KNN} is the probability that a B atom is a KNN of an A atom, and x_B is B's atom fraction in the region (A,B=Ge,Sn). For a random alloy, $\alpha_{Sn-Sn}^{KNN} = 1$. On the contrary, $\alpha_{Sn-Sn}^{KNN} > 1$ (or < 1) means a higher (or lower) preference for an Sn atom to be surrounded by other Sn atoms in its KNN shell compared to a random alloy.

Note that our definition of SRO parameter in Equation (1) is exactly equal to 1 minus the Warren-Cowley SRO parameter commonly used in theoretical literature. This experimental definition in Equation (1) is used in this paper because it more intuitively correlates a larger SRO parameter with the preference for A-B KNN.

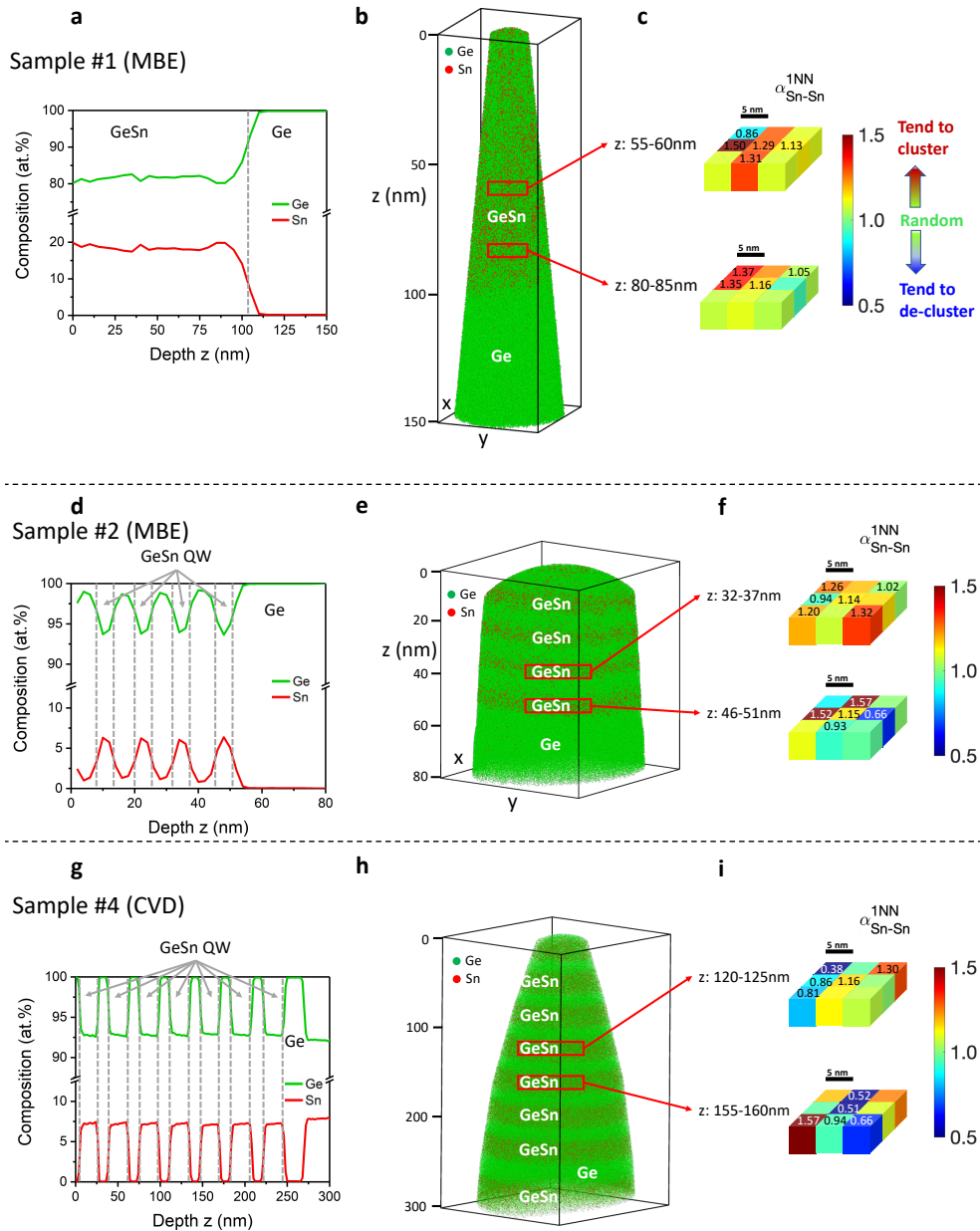


Fig. 1 APT data. a) Composition profile in sample #1. b) Reconstructed APT data of sample #1. c) SRO mapping examples in GeSn region in sample #1. d) Composition profile in sample #2. e) Reconstructed APT data of sample #2. f) SRO mapping examples in GeSn region in sample #2. g) Composition profile in sample #4. h) Reconstructed APT data of sample #4. i) SRO mapping examples in GeSn region in sample #4.

2.3 Robustness of the Poisson-KNN Method for SRO Analyses

In order to extract the true KNN (K^{th} nearest neighbor) shell information from the APT data with atomic position perturbations, the Poisson-KNN method developed in Ref.[30] was used to reconstruct the true KNN shells by a statistically weighted sum of nominal KNN in the APT data. As a physics-informed statistical method, this Poisson-KNN approach incorporates the number of KNNs for a given atom in the corresponding crystal structure, as well as the detection efficiency from the experimental APT data. The number of A-B pairs in each true KNN shell was also weighted summed by the A-B pairs in the nominal KNN shells. Then P_{A-B}^{KNN} was calculated as the ratio between the number of A-B pairs and the total number of A-all pairs in the true KNN shell. To reach statistical significance, nanocubes of $5 \text{ nm} \times 5 \text{ nm} \times 5 \text{ nm}$ size were chosen in this paper to calculate local SRO parameters in each nanocube and map the spatial distribution of SRO. Approximately 2000 atoms in each nanocube are sufficient for statistical analysis.

To test the robustness of this Poisson-KNN method in distinguishing SRO from random alloys, theoretically simulated supercell ($11.7 \times 11.7 \times 11.7 \text{ nm}^3$) data of a random $Ge_{0.75}Sn_{0.25}$ alloy and a $Ge_{0.75}Sn_{0.25}$ alloy with SRO (of Sn-Sn repulsion as predicted in Ref.[23]) were generated based on the recently developed machine-learning potential of GeSn which has been shown to offer the level of accuracy of density functional theory.[25] To simulate the actual detection efficiency and the spatial error of measuring atomic positions in real APT data, 50% percent of atoms were removed randomly, and spatial perturbations of atomic position were introduced to the theoretically modelled perfect $Ge_{0.75}Sn_{0.25}$ supercell following a Gaussian distribution [34] with a standard deviation of 1-3 Å. For a $Ge_{0.75}Sn_{0.25}$ alloy with SRO, the true α_{Sn-Sn}^{1NN} of the perfect supercell is 0.22, and Poisson-KNN method gives 0.53 and 0.82 when the standard deviation of atomic perturbation is 1 Å and 3 Å, respectively, still well distinguished from random alloys, as shown in Figure 2a. Note that 3 Å atomic displacement is approximately 2x greater than the difference in radii between 1NN and 2NN shells (1.61 Å), indicating that the statistical Poisson-KNN method is quite robust in identifying Sn-Sn SRO even with relatively large spatial perturbations. In contrast, for a random $Ge_{0.75}Sn_{0.25}$ alloy with true α_{Sn-Sn}^{1NN} of 1, Poisson-KNN method gets 0.97-0.99 when atomic perturbation ranges from 1-3 Å, proving this method can successfully distinguish a random $Ge_{0.75}Sn_{0.25}$ alloy from a $Ge_{0.75}Sn_{0.25}$ alloy with α_{Sn-Sn}^{1NN} SRO of 0.22 even when the atomic displacement is as large as 3 Å.

Another important takeaway is APT could underestimate SRO due to atomic position perturbation, and the measured SRO is a function of the magnitude of the perturbation. Thus, to make a fair comparison between SRO derived from different APT data, it is critical to evaluate the atomic perturbation in these APT data. In figure 2b, we confirm that the standard deviation of reconstructed true 1NN distance distribution in all four sets of APT data for MBE and CVD samples are almost identical ($\sim 1.1 \text{ Å}$) with a variation smaller than 0.1 Å among them, indicating the atomic perturbation is almost the same in the APT data of all 4 samples. Therefore, the relative comparison between MBE and CVD SRO parameters using Poisson-KNN method is well validated.

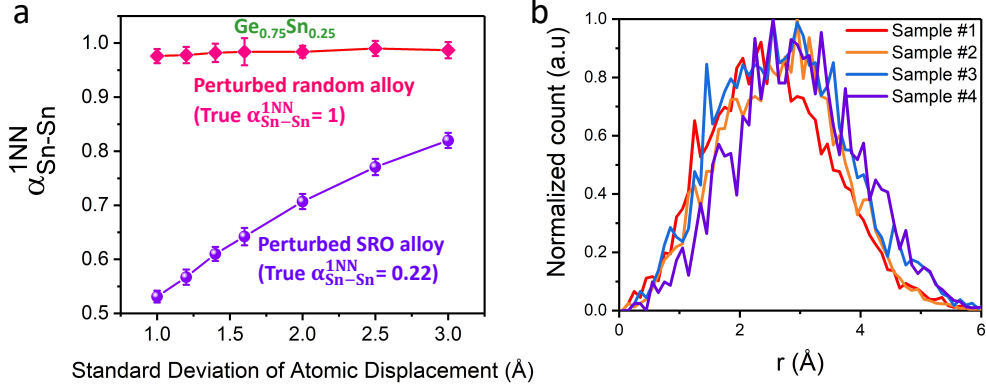


Fig. 2 a) Sn-Sn 1NN SRO in theoretically simulated supercell data calculated using Poisson-KNN method. Red curve: a random $\text{Ge}_{0.75}\text{Sn}_{0.25}$ alloy with true $\alpha_{\text{Sn-Sn}}^{1\text{NN}} = 1$. Purple curve: a $\text{Ge}_{0.75}\text{Sn}_{0.25}$ alloy with SRO, $\alpha_{\text{Sn-Sn}}^{1\text{NN}} = 0.22$. b) Normalized histogram of reconstructed true 1NN distance in 4 samples. The standard deviation is 1.05, 1.04, 1.12, 1.08 Å for sample #1-4, respectively.

2.4 SRO results

Sn-Sn 1NN SRO maps with a $5 \text{ nm} \times 5 \text{ nm} \times 5 \text{ nm}$ spatial resolution were produced and exemplified in Fig. 1c, f and i. More cubes with $\alpha_{\text{Sn-Sn}}^{1\text{NN}}$ larger than 1.2 can be found in sample #1 and #2, while more cubes with $\alpha_{\text{Sn-Sn}}^{1\text{NN}}$ lower than 0.8 can be found in sample #4. Therefore, MBE samples show signs of more preference for Sn-Sn 1NN than CVD samples.

Histograms of the Sn-Sn 1NN SRO $\alpha_{\text{Sn-Sn}}^{1\text{NN}}$ in these four samples are compared in Fig. 3. Red color is used for MBE samples and blue color represents CVD samples. In these four samples, 72, 100, 250, and 200 nanocubes were analyzed, with the mean values and standard deviations of the $\alpha_{\text{Sn-Sn}}^{1\text{NN}}$ labeled next to the histograms. The Gaussian fitting curve of each histogram is also shown in Fig. 3. A notable distinction is that the MBE samples have a larger $\alpha_{\text{Sn-Sn}}^{1\text{NN}}$, indicating a stronger preference of Sn-Sn 1NN. In particular, almost 90% of the nanocubes in MBE sample #1 (63 out of 72) and 66% of those in sample #2 (66 out of 100) showed Sn-Sn 1NN SRO parameters greater than 1. The average $\alpha_{\text{Sn-Sn}}^{1\text{NN}}$ is 1.14 for both sample #1 and #2, while it is ~ 1.01 for sample #3 and #4. This means MBE samples have $\sim 15\%$ stronger preference for Sn-Sn 1NN compared to CVD samples. Note that $\alpha_{\text{Sn-Sn}}^{1\text{NN}}$ in sample #2 and #4 has a larger standard deviation because the Sn composition is lower such that less Sn-Sn 1NN pairs are available for statistical analyses in each nanocube.

Sn-Sn 1NN SRO and Sn composition of all four samples are summarized in Fig. 4. The center squares and bars are averaged $\alpha_{\text{Sn-Sn}}^{1\text{NN}}$ and their standard deviations to represent the statistical distribution. The triangles are Sn composition. Data points of MBE and CVD samples are filled in red and blue color, respectively. Again, it is clear that Sn-Sn 1NN SRO is higher for MBE samples, and this difference is independent of the Sn composition. Furthermore, as discussed earlier in Fig. 2b, the degree of atomic site perturbation is similar across all 4 samples in the APT measurements. This is further confirmed by the data in Fig. S1 in the Supporting Information, showing that

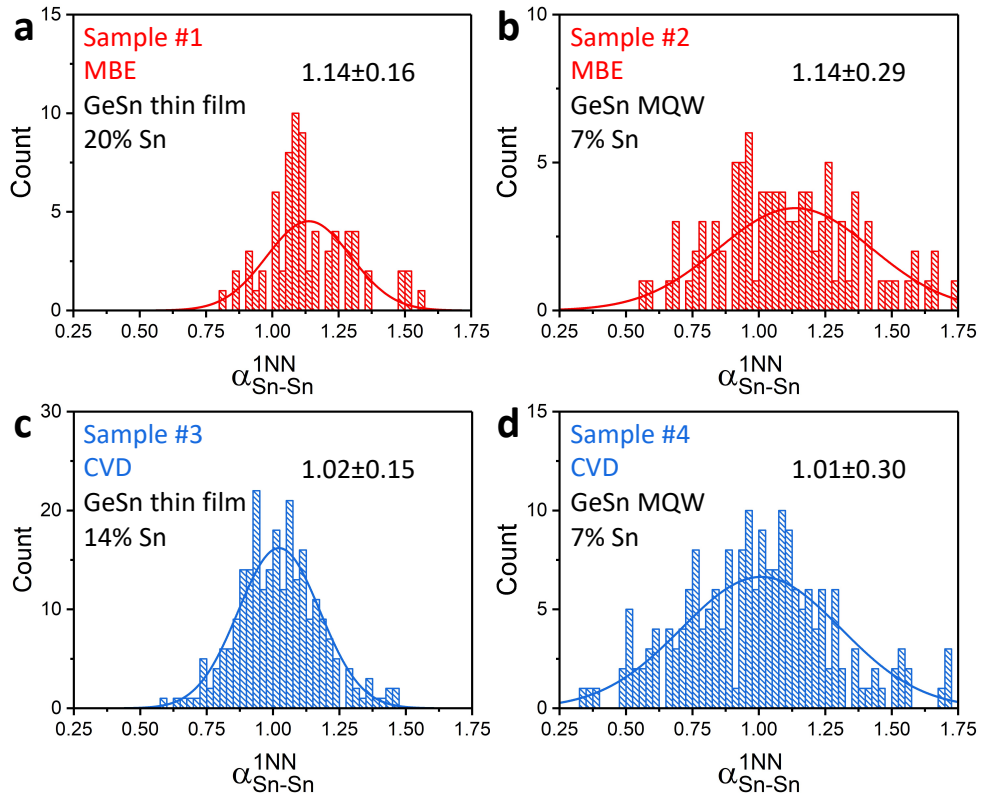


Fig. 3 Histogram of Sn-Sn 1NN SRO α_{Sn-Sn}^{1NN} in four samples. Sample size = 72, 100, 250, and 200 (nanocubes) for these four samples.

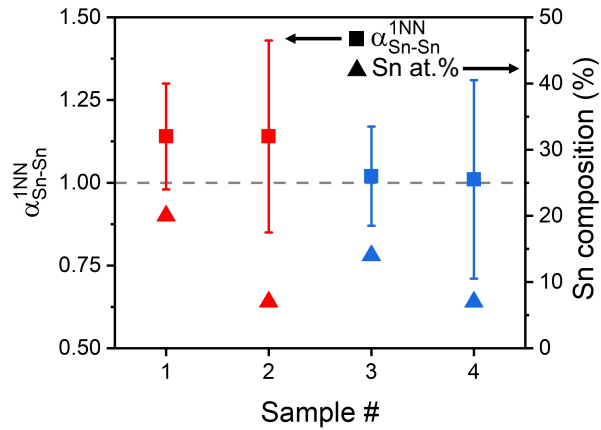


Fig. 4 Summary of Sn-Sn 1NN SRO α_{Sn-Sn}^{1NN} and Sn composition

the Sn-Sn 1NN SRO parameter is independent of the Ge⁺/Ge⁺⁺ ratios in the APT data collection, a measure of the contribution of laser evaporation relative to the field evaporation process. Overall, we find that the observed difference between Sn-Sn 1NN SRO parameters between MBE and CVD is independent composition or APT measurement conditions.

Another striking observation is that the difference in Sn-Sn 1NN SRO between MBE and CVD samples also holds true irrespective of the growth tools. As mentioned earlier, the two MBE samples are grown by different tools at two different research labs, yet the SRO parameters are strikingly similar despite the differences in the detailed growth conditions, both showing $\sim 15\%$ stronger preference of Sn-Sn 1NN than their CVD counterparts. The same is true for the two CVD samples grown by two very different reactors. Therefore, the differences in SRO parameters between MBE and CVD is most likely due to fundamentally different growth mechanisms between MBE and CVD. This will be discussed in the next section.

2.5 First-principles calculations

Considering there is no surface termination in MBE (ultrahigh vacuum), unlike the H-terminated surface in CVD, we hypothesize that the surface chemistry and kinetics of precursors may play a significant role in determining the final SRO. To verify this hypothesis, we did first-principles calculations on the energy of Sn-Sn in the top three layers at the growth front with and without H termination. The first-principles calculations were performed with Perdew-Burke-Ernzerhof (PBE) functional in the Vienna Ab initio Simulation Package (VASP) [35] based on the projector augmented wave method.[36] A $16.4 \text{ \AA} \times 16.4 \text{ \AA} \times 34.7 \text{ \AA}$ supercell with 13 atomic layer of Ge along (001) direction, which is the same as the growth directions of the samples, and 17 \AA vacuum along z axis is applied. The x-y lattice constant is fixed to the fully relaxed lattice constant of Ge bulk ($\sim 5.78 \text{ \AA}$). The top layer is applied to investigate the interaction between Sn atoms and the lower surface is fully passivated by adding two H atoms to each Ge atom. The H and lowest Ge layer is fixed to avoid additional strain effect. An energy cutoff of 300 eV and a $4 \times 4 \times 1$ Monkhorst-Pack k-points grid are chosen for structural relaxation, combined with the convergence criteria of 10^{-6} and 5×10^{-3} eV for electronic and ionic relaxations, respectively.

In MBE growth without surfactant, the growth front is considered a free surface, as shown in Figure 5a. Each atom on the surface holds two dangling electrons. One of these bonds is stabilized through the formation of a dimer with a neighboring surface atom. The two remaining dangling bonds from each dimer pair distributed to 1 side leads to the buckling of the dimers. To reduce the strain energy, the adjacent surface dimers are buckled in opposite way, leading to the p(2 \times 2) surface reconstruction [37] shown in Figure 5b. According to the symmetry, the atomic sites near the surface can be classified into 5 types as labeled in Figure 5a. For chemical vapor deposition (CVD), the precursor and the carrier gas can include hydrogen atoms, so the top surface is hydrogenated. As shown in Figure 5c, d, the hydrogen atoms passivate all the unpaired electrons in the surface dimer, so the buckling of the dimers disappears, therefore, the 1A and 1B atomic site in Figure 5a becomes equivalent and relabeled as 1 in Figure 5c.

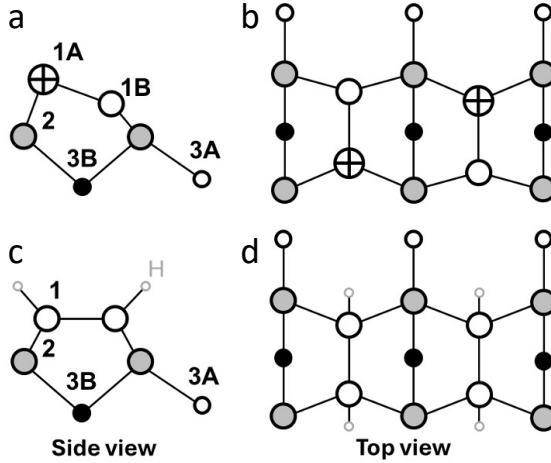


Fig. 5 The a) side and b) top view of atomic structures for the free surface with $p(2 \times 2)$ reconstruction. The c) side and d) top view of atomic structures with nonhydrogenated surface. The little grey circle represents the hydrogen atom and others represent Ge or Sn atoms. Different patterns of atoms represent different classes if equivalent sites.

During the growth process, with a low defect density, Sn atoms in the Ge bulk exhibit a high diffusion barrier (~ 3.2 eV), even when mediated by vacancies.[38] Thus, their position is hard to change under the standard growth temperature (~ 150 °C for MBE and ~ 300 °C for CVD). However, previous experiments have shown that the diffusion barrier for Sn near the top surface of GeSn and SiGeSn alloy can be less than 1 eV,[39, 40] which allows the Sn atoms to rearrange themselves within this region. Assume the Sn diffusion mainly happens between surface and sub-surface, the interaction between Sn atoms in the top three layers can play an important role in the formation of SRO. In this calculation, we focus on the interaction between Sn atoms within 1NN shell

The interaction between Sn atoms can be quantitatively characterized by the energy change (ΔE) when two isolated Sn atoms are brought together to form a 1NN bond. This interaction is repulsive when ΔE is positive and attractive when ΔE is negative. Since the energy of the system is different when a Sn atom occupies different class of atomic sites labeled in Figure 5, the Sn atoms must occupy the same class of atomic sites for both isolated and 1NN cases to make the energy comparable. For MBE growth, Sn has a strong tendency to segregate to the top surface,[41] and previous experiment has shown that the growth front tends to have higher Sn concentration,[42] so we assume the surface (1A and 1B sites) are fully occupied by Sn atoms. Then only the interaction between Sn in 2nd and 3rd layer from top surface should be considered. As shown in left panel of Figure 6, all symmetry inequivalent sites for Sn-Sn dimers are labeled as M1 (between sites 2 and 3B) and M2 (between sites 2 and 3A). Energy calculations show that Sn atoms in the M1 configuration are attractive (negative ΔE), whereas those in the M2 configuration are repulsive (positive ΔE).

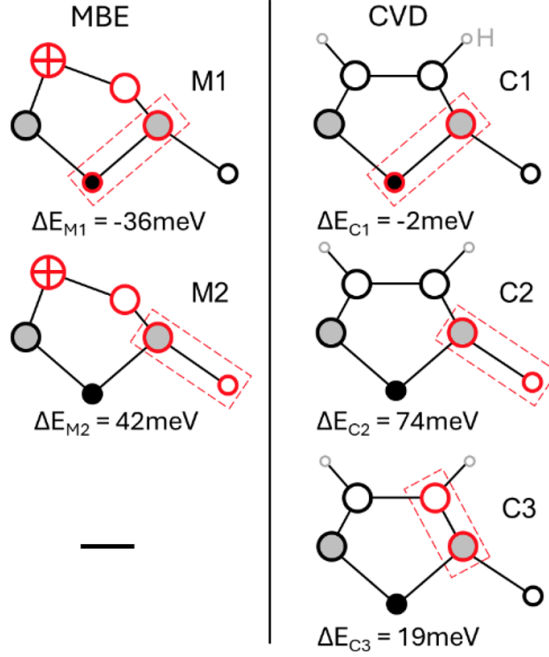


Fig. 6 The interaction between Sn atoms in 1st neighbor shell with different configurations for MBE (left) and CVD (right) near the top surface. The atomic site occupied by Sn is highlighted by red color and all other sites are Ge. The Sn-Sn dimer where ΔE is calculated is highlighted by red dash box.

For CVD growth, where the surface is hydrogenated, the Sn segregation can be suppressed.[41] Then all possible configurations of Sn-Sn dimers within the top three layers should be considered, including configurations C1 and C2 which correspond to M1 and M2 in MBE growth, respectively. By comparing the ΔE_{C1} with ΔE_{M1} or ΔE_{C2} with ΔE_{M2} , it shows a tendency that H atoms can enhance the repulsion between Sn atoms by ~ 35 meV. Additionally, there is a new C3 configuration for Sn-Sn dimer between sites 1 and 2, which also shows repulsive interactions between Sn atoms. Therefore, the hydrogenated surface in CVD growth can lead to less preference for Sn-Sn 1NN than MBE driven by stronger repulsive interaction between Sn atoms. This is consistent with experimental results. We will publish the detailed theoretical study in another paper.

2.6 Discussion

GeSn thin films of similar compositions (20% and 14% Sn) and GeSn MQWs of an identical composition (7% Sn) grown by MBE and CVD were systematically compared in this study. Statistic analysis reveals that MBE GeSn samples favors Sn-Sn 1NN more than their CVD counterparts for both thin film and MQW cases, irrespective of the growth tools. Real-space nano-scale SRO mappings and distributions of MBE GeSn samples are reported here for the first time, giving us a better understanding of the difference between CVD and MBE for GeSn growth. It has been demonstrated

that the averaged SRO is not enough to represent the entire structure that determines the properties of SiGeSn alloy system[29]. Therefore, a technique such as APT that can characterize the distribution of SRO is necessary.

Echoing with the experimental results on Sn-Sn 1NN SRO analyses, the theoretical work also shows that reconstructed GeSn surface in vacuum (as in the case of MBE) tends to favor Sn-Sn 1NN at the growth front (as indicated by the negative ΔE_{M1} in Figure 6). This also leads to a stronger tendency of Sn segregation on the surface. On the other hand, the modeling also shows that H passivation, as usually occurs in CVD, helps to reduce Sn-Sn 1NN preference at the growth front and suppress Sn surface segregation. This finding qualitatively explains the drastic difference in the growth temperature windows between MBE and CVD—the former has a stronger preference of Sn-Sn 1NN near the surface, therefore a lower growth temperature is needed to suppress Sn surface segregation at the growth front.

Overall, our result also points to surface termination engineering to control Sn-Sn SRO in GeSn thin films. Similarly, it has been reported that surfactant can affect SRO in other systems like GaAsSb and GaAsN.[43, 44]. Notably, in the case of ternary SiGeSn alloys, SRO has been predicted to play a critical role on the band structures.[29, 45] Therefore, extending surface termination engineering to SiGeSn may offer a new degree of freedom for band engineering via SRO control.

Last but not least, the difference in SRO may also impact defect formation in GeSn and SiGeSn thin films. Recent studies in HEAs showed that SRO can affect dislocations.[46–49] The mobility of edge dislocation is enhanced by SRO in MoNbTaW [50] while reduced by SRO in CrCoNi [51]. From this perspective, we could hypothesize that SRO may affect the nucleation and gliding of dislocation in GeSn, leading to the different strain relaxation observed in MBE GeSn and CVD GeSn. Our ongoing work also shows a drastic impact of SRO on vacancy formation energy, with details to be presented in another paper. The correlation between SRO and defects will be further explored, as it may give a direction to control the strain relaxation in GeSn to achieve better growth quality for optoelectronic devices.

3 Conclusion

In summary, SRO in GeSn grown by MBE and CVD has been analyzed using APT. Approximately 15% stronger preference of Sn-Sn 1NN (based on SRO parameters) is observed in MBE GeSn than CVD GeSn, which is consistent with the theoretical prediction that surfaces with and without H termination can reduce or enhance the preference of Sn-Sn 1NN. This finding not only suggests engineering surface termination or surfactants during the growth as a potential approach to control SRO in GeSn and SiGeSn alloys as a potentially new degree of freedom for band engineering, but also provides some insight into the underlying reasons for very different growth temperature windows between MBE and CVD that directly impact the strain relaxation behavior.

4 Experimental Section

APT measurement conditions: APT data were collected using pulse laser energies ranging from 5 to 75 pJ. Detailed measurement conditions for the four samples are provided in Table S1 in the supporting information. The reconstructions were performed using Cameca IVAS software.

Statistical analysis: SRO was calculated for each $5 \times 5 \times 5 \text{ nm}^3$ nanocube, with each nanocube containing $\sim 2,000$ atoms to ensure statistically significant results. The number of nanocubes analyzed for the four samples were 72, 100, 250, and 200, respectively, providing sufficient data for statistical analysis.

Programming: The Poisson-KNN method programs were written using Python.[30] APT data was imported by Python package “apt-tools”.[52]

Supplementary information. APT measurement conditions.

Acknowledgments. The Poisson-KNN method of analyzing SRO from the APT data had been developed under the support of the Air Force Office of Scientific Research under the award number FA9550-19-1-0341. The APT tip preparation and data collection of the GeSn samples provided by University of Arkansas and University of Delaware, the DFT computational modeling of MBE vs. CVD growths, and the supercell modeling of APT data have been supported by μ -ATOMS, an Energy Frontier Research Center funded by the U.S. Department of Energy (DOE), Office of Science, Basic Energy Sciences (BES), under the award DE-SC0023412.

Declarations

- Conflict of interest/Competing interests
The authors declare no conflict of interest.
- Availability of data and materials
The data that support the findings of this study are available from the corresponding author upon reasonable request.
- Code availability
The code are available from the corresponding author upon reasonable request.
- Authors’ contributions
J.L. conceived this work. S.L. calculated SRO from APT data. Y.L. and S.Z. performed DFT total-energy calculations. A.C. and X.W. analyzed data. J.B., I.B., C.C., A.A. conducted APT data acquisition and reconstruction. X.J., S.C. and T.L. generated theoretical GeSn supercell data to test the robustness of our method. H.Z., N.E., O.C., Y.Z., D.B., G.S. and S.Y. provided GeSn samples.

References

- [1] Wirths, S., Geiger, R., Von Den Driesch, N., Mussler, G., Stoica, T., Mantl, S., Ikonik, Z., Luysberg, M., Chiussi, S., Hartmann, J.-M., *et al.*: Lasing in direct-bandgap gesn alloy grown on si. *Nature photonics* **9**(2), 88–92 (2015)

- [2] Homewood, K.P., Lourenço, M.A.: The rise of the gesn laser. *Nature Photonics* **9**(2), 78–79 (2015)
- [3] Kim, Y., Assali, S., Joo, H.-J., Koelling, S., Chen, M., Luo, L., Shi, X., Burt, D., Ikonik, Z., Nam, D., *et al.*: Short-wave infrared cavity resonances in a single gesn nanowire. *Nature Communications* **14**(1), 4393 (2023)
- [4] Zhou, Y., Ojo, S., Wu, C.-W., Miao, Y., Tran, H., Grant, J.M., Abernathy, G., Amoah, S., Bass, J., Salamo, G., *et al.*: Electrically injected gesn lasers with peak wavelength up to 2.7 μm . *Photonics Research* **10**(1), 222–229 (2022)
- [5] Margetis, J., Al-Kabi, S., Du, W., Dou, W., Zhou, Y., Pham, T., Grant, P., Ghetmiri, S., Mosleh, A., Li, B., *et al.*: Si-based gesn lasers with wavelength coverage of 2–3 μm and operating temperatures up to 180 k. *ACs Photonics* **5**(3), 827–833 (2017)
- [6] Talamas Simola, E., Kiyek, V., Ballabio, A., Schlykow, V., Frigerio, J., Zucchetti, C., De Iacovo, A., Colace, L., Yamamoto, Y., Capellini, G., *et al.*: Cmos-compatible bias-tunable dual-band detector based on gesn/ge/si coupled photodiodes. *ACS photonics* **8**(7), 2166–2173 (2021)
- [7] Tran, H., Pham, T., Margetis, J., Zhou, Y., Dou, W., Grant, P.C., Grant, J.M., Al-Kabi, S., Sun, G., Soref, R.A., *et al.*: Si-based gesn photodetectors toward mid-infrared imaging applications. *ACS Photonics* **6**(11), 2807–2815 (2019)
- [8] Chen, Q., Zhou, H., Xu, S., Huang, Y.-C., Wu, S., Lee, K.H., Gong, X., Tan, C.S.: A route toward high-detectivity and low-cost short-wave infrared photodetection: Gesn/ge multiple-quantum-well photodetectors with a dielectric nanohole array metasurface. *ACS nano* (2023)
- [9] Elbaz, A., Arefin, R., Sakat, E., Wang, B., Herth, E., Patriarche, G., Foti, A., Ossikovski, R., Sauvage, S., Checoury, X., *et al.*: Reduced lasing thresholds in gesn microdisk cavities with defect management of the optically active region. *ACS photonics* **7**(10), 2713–2722 (2020)
- [10] Elbaz, A., Buca, D., Driesch, N., Pantzas, K., Patriarche, G., Zerounian, N., Herth, E., Checoury, X., Sauvage, S., Sagnes, I., *et al.*: Ultra-low-threshold continuous-wave and pulsed lasing in tensile-strained gesn alloys. *Nature Photonics* **14**(6), 375–382 (2020)
- [11] Dou, W., Benamara, M., Mosleh, A., Margetis, J., Grant, P., Zhou, Y., Al-Kabi, S., Du, W., Tolle, J., Li, B., *et al.*: Investigation of gesn strain relaxation and spontaneous composition gradient for low-defect and high-sn alloy growth. *Scientific reports* **8**(1), 5640 (2018)
- [12] Atalla, M.R., Assali, S., Koelling, S., Attiaoui, A., Moutanabbir, O.: Dark current in monolithic extended-swir gesn pin photodetectors. *Applied Physics Letters*

- [13] Liu, X., Zheng, J., Niu, C., Liu, T., Huang, Q., Li, M., Zhang, D., Pang, Y., Liu, Z., Zuo, Y., *et al.*: Sn content gradient gesn with strain controlled for high performance gesn mid-infrared photodetectors. *Photonics Research* **10**(7), 1567–1574 (2022)
- [14] Zhang, L., Song, Y., Driesch, N., Zhang, Z., Buca, D., Grützmacher, D., Wang, S.: Structural property study for gesn thin films. *Materials* **13**(16), 3645 (2020)
- [15] Wang, N., Xue, C., Wan, F., Zhao, Y., Xu, G., Liu, Z., Zheng, J., Zuo, Y., Cheng, B., Wang, Q.: Spontaneously conversion from film to high crystalline quality stripe during molecular beam epitaxy for high sn content gesn. *Scientific Reports* **10**(1), 6161 (2020)
- [16] Oehme, M., Schmid, M., Kaschel, M., Gollhofer, M., Widmann, D., Kasper, E., Schulze, J.: Gesn pin detectors integrated on si with up to 4% sn. *Applied Physics Letters* **101**(14) (2012)
- [17] Miao, Y., Wang, G., Kong, Z., Xu, B., Zhao, X., Luo, X., Lin, H., Dong, Y., Lu, B., Dong, L., *et al.*: Review of si-based gesn cvd growth and optoelectronic applications. *Nanomaterials* **11**(10), 2556 (2021)
- [18] Margetis, J., Mosleh, A., Al-Kabi, S., Ghetmiri, S.A., Du, W., Dou, W., Benamara, M., Li, B., Mortazavi, M., Naseem, H., *et al.*: Study of low-defect and strain-relaxed gesn growth via reduced pressure cvd in h2 and n2 carrier gas. *Journal of Crystal Growth* **463**, 128–133 (2017)
- [19] Dou, W., Alharthi, B., Grant, P.C., Grant, J.M., Mosleh, A., Tran, H., Du, W., Mortazavi, M., Li, B., Naseem, H., *et al.*: Crystalline gesn growth by plasma enhanced chemical vapor deposition. *Optical Materials Express* **8**(10), 3220–3229 (2018)
- [20] Rathore, J., Nanwani, A., Mukherjee, S., Das, S., Moutanabbir, O., Mahapatra, S.: Composition uniformity and large degree of strain relaxation in mbe-grown thick gesn epitaxial layers, containing 16% sn. *Journal of Physics D: Applied Physics* **54**(18), 185105 (2021)
- [21] Imbrenda, D., Hickey, R., Carrasco, R.A., Fernando, N.S., VanDerslice, J., Zollner, S., Kolodzey, J.: Infrared dielectric response, index of refraction, and absorption of germanium-tin alloys with tin contents up to 27% deposited by molecular beam epitaxy. *Applied Physics Letters* **113**(12) (2018)
- [22] Wan, F., Xu, C., Wang, X., Xu, G., Cheng, B., Xue, C.: Study of strain evolution mechanism in ge1-xsnx materials grown by low temperature molecular beam epitaxy. *Journal of Crystal Growth* **577**, 126399 (2022)

- [23] Cao, B., Chen, S., Jin, X., Liu, J., Li, T.: Short-range order in gesn alloy. *ACS Applied Materials & Interfaces* **12**(51), 57245–57253 (2020)
- [24] Chen, S., Li, T.: Impacts of short-range order on thermal conductivity of si-ge-sn alloys. *APS March Meeting 2023*, Volume 68, Number 3, Paper F61.00008 (<https://meetings.aps.org/Meeting/MAR23/Session/F61.8>)
- [25] Chen, S., Jin, X., Zhao, W., Li, T.: Intricate short-range order in gesn alloys revealed by atomistic simulations with highly accurate and efficient machine-learning potentials. *Physical Review Materials* **8**(4), 043805 (2024)
- [26] Gencarelli, F., Grandjean, D., Shimura, Y., Vincent, B., Banerjee, D., Vantomme, A., Vandervorst, W., Loo, R., Heyns, M., Temst, K.: Extended x-ray absorption fine structure investigation of sn local environment in strained and relaxed epitaxial ge_{1-x}sn_x films. *Journal of Applied Physics* **117**(9) (2015)
- [27] Lentz, J.Z., Woicik, J., Bergschneider, M., Davis, R., Mehta, A., Cho, K., McIntyre, P.C.: Local ordering in ge/ge-sn semiconductor alloy core/shell nanowires revealed by extended x-ray absorption fine structure (exafs). *Applied Physics Letters* **122**(6) (2023)
- [28] Soo, Y., Wu, T., Chen, Y., Shiu, Y., Peng, H., Tsai, Y., Liao, P., Zheng, Y., Chang, S., Chan, T., *et al.*: Substitutional incorporation of sn in compressively strained thin films of heavily-alloyed ge_{1-x}sn_x/ge semiconductor probed by x-ray absorption and diffraction methods. *Semiconductor Science and Technology* **29**(11), 115008 (2014)
- [29] Jin, X., Chen, S., Lemkan, C., Li, T.: Role of local atomic short-range order distribution in alloys: Why it matters in si-ge-sn alloys. *Physical Review Materials* **7**(11), 111601 (2023)
- [30] Liu, S., Covian, A.C., Wang, X., Cline, C.T., Akey, A., Dong, W., Yu, S.-Q., Liu, J.: 3d nanoscale mapping of short-range order in gesn alloys. *Small Methods* **6**(5), 2200029 (2022)
- [31] Vurpillot, F., Da Costa, G., Menand, A., Blavette, D.: Structural analyses in three-dimensional atom probe: a fourier transform approach. *Journal of Microscopy* **203**(3), 295–302 (2001)
- [32] Zhou, J., Odqvist, J., Thuvander, M., Hedström, P.: Quantitative evaluation of spinodal decomposition in fe-cr by atom probe tomography and radial distribution function analysis. *Microscopy and Microanalysis* **19**(3), 665–675 (2013)
- [33] Moody, M.P., Gault, B., Stephenson, L.T., Haley, D., Ringer, S.P.: Qualification of the tomographic reconstruction in atom probe by advanced spatial distribution map techniques. *Ultramicroscopy* **109**(7), 815–824 (2009)

- [34] Gault, B., Moody, M.P., Cairney, J.M., Ringer, S.P.: Atom Probe Microscopy vol. 160. Springer, New York (2012)
- [35] Kresse, G., Furthmüller, J.: Efficient iterative schemes for ab initio total-energy calculations using a plane-wave basis set. *Physical review B* **54**(16), 11169 (1996)
- [36] Blöchl, P.E.: Projector augmented-wave method. *Physical review B* **50**(24), 17953 (1994)
- [37] Zandvliet, H.J.: The $ge(0\ 0\ 1)$ surface. *Physics reports* **388**(1), 1–40 (2003)
- [38] Chroneos, A., Bracht, H., Grimes, R., Uberuaga, B.P.: Vacancy-mediated dopant diffusion activation enthalpies for germanium. *Applied Physics Letters* **92**(17) (2008)
- [39] Li, H., Chang, C., Chen, T., Cheng, H., Shi, Z., Chen, H.: Characteristics of sn segregation in ge/ge_{sn} heterostructures. *Applied Physics Letters* **105**(15) (2014)
- [40] Taoka, N., Asano, T., Yamaha, T., Terashima, T., Nakatsuka, O., Costina, I., Zaumseil, P., Capellini, G., Zaima, S., Schroeder, T.: Non-uniform depth distributions of sn concentration induced by sn migration and desorption during $gesni$ layer formation. *Applied Physics Letters* **106**(6) (2015)
- [41] Johll, H., Samuel, M., Koo, R.Y., Kang, H.C., Yeo, Y.-C., Tok, E.S.: Influence of hydrogen surface passivation on sn segregation, aggregation, and distribution in $gesn/ge(001)$ materials. *Journal of Applied Physics* **117**(20) (2015)
- [42] Wegscheider, W., Olajos, J., Menczigar, U., Dondl, W., Abstreiter, G.: Fabrication and properties of epitaxially stabilized ge/α -sn heterostructures on $ge(001)$. *Journal of crystal growth* **123**(1-2), 75–94 (1992)
- [43] Jiang, W., Liu, J., So, M., Rao, T., Thewalt, M., Kavanagh, K., Watkins, S.: Effect of bi surfactant on atomic ordering of ga_{sn} . *Applied physics letters* **85**(23), 5589–5591 (2004)
- [44] Occena, J., Jen, T., Lu, H., Carter, B., Jimson, T., Norman, A., Goldman, R.: Surfactant-induced chemical ordering of ga_{sn} : Bi. *Applied Physics Letters* **113**(21), 211602 (2018)
- [45] Jin, X., Chen, S., Li, T.: Coexistence of two types of short-range order in si - ge - sn medium-entropy alloys. *Communications Materials* **3**(1), 66 (2022)
- [46] Zhang, R., Zhao, S., Ding, J., Chong, Y., Jia, T., Ophus, C., Asta, M., Ritchie, R.O., Minor, A.M.: Short-range order and its impact on the cr_{con} medium-entropy alloy. *Nature* **581**(7808), 283–287 (2020)
- [47] Zhang, R., Zhao, S., Ophus, C., Deng, Y., Vachhani, S.J., Ozdol, B., Traylor, R., Bustillo, K.C., Morris Jr, J., Chrzan, D.C., *et al.*: Direct imaging of short-range

- order and its impact on deformation in ti-6al. *Science advances* **5**(12), 2799 (2019)
- [48] Ma, S., Zhang, J., Xu, B., Xiong, Y., Shao, W., Zhao, S.: Chemical short-range ordering regulated dislocation cross slip in high-entropy alloys. *Journal of Alloys and Compounds* **911**, 165144 (2022)
- [49] Neeraj, T., Mills, M.: Short-range order (sro) and its effect on the primary creep behavior of a ti-6wt.% al alloy. *Materials Science and Engineering: A* **319**, 415–419 (2001)
- [50] Yin, S., Zuo, Y., Abu-Odeh, A., Zheng, H., Li, X.-G., Ding, J., Ong, S.P., Asta, M., Ritchie, R.O.: Atomistic simulations of dislocation mobility in refractory high-entropy alloys and the effect of chemical short-range order. *Nature communications* **12**(1), 4873 (2021)
- [51] Tian, Y., Chen, F.: Short-range order-dependent dislocation mobilities in crconi medium entropy alloy: Atomistic simulations and modeling. *International Journal of Plasticity* **172**, 103859 (2024)
- [52] Branson, O.: apt-tools. GitHub (2016)